PERGAMON

International Journal of Solids and Structures 40 (2003) 1243–1264

INTERNATIONAL JOURNAL OF SOLIDS and STRUCTURES

www.elsevier.com/locate/ijsolstr

Characterization of anisotropy in porous media by means of linear intercept measurements

D. Inglis, S. Pietruszczak *

Department of Civil Engineering and Engineering Mechanics, McMaster University, 1280 Main St. West, Hamilton, Ont., Canada L8S 4L7

Received 15 September 2001; received in revised form 17 October 2002

Abstract

The focus of this paper is the description and identification of the anisotropic microstructure of porous media. To begin, a general discussion on fabric descriptors employing linear intercept measurements is provided and a new fabric measure, referred to as areal pore size distribution, is proposed. Subsequently, the issue of the identification of fabric descriptors is addressed and fabric detection algorithms, incorporating 3D computed tomography images, are described. Finally, examples of identification of the microstructure of trabecular bone samples are provided and the performance of different fabric descriptors is assessed.

Keywords: Anisotropy; Microstructure; Fabric tensor; Computed tomography; Trabecular bone

1. Introduction

Porous materials are often anisotropic. The anisotropy stems primarily from the arrangement of porous microstructure and manifests itself in the directional dependence of both mechanical characteristics and flow properties. In a number of naturally occurring and manufactured materials (sedimentary rocks and soils, reinforced composites, etc.) the principal material directions are known a priori. In this case, the formulation of the problem may be simplified by employing structure-orientation tensors, which represent the dyadic products of the material triad (e.g., Pietruszczak and Mroz, 2001). On the other hand however, materials with complex architecture (e.g., trabecular bone) or those experiencing deformation induced anisotropy require, in general, some explicit measures of fabric. The latter issue, i.e., that of quantification of fabric, is the main focus of this paper.

Fabric detection algorithms usually employ the basic principles of stereology. Typically, three-dimensional (3D) parameters of interest are estimated by sampling in a statistical sense with two-dimensional (2D) or one-dimensional (1D) geometric entities. The procedures incorporating stereologic principles have

* Corresponding author. Tel.: +1-905-525-9140; fax: +1-905-529-9688.
E-mail address: pietrusz@mcmaster.ca (S. Pietruszczak).

0020-7683/02/$ - see front matter
PII: S0020-7683(02)00595-4

been widely used in the area of bone mechanics. For example, Whitehouse (1974) developed stereological measurement techniques incorporating lineal probes for describing the anisotropy of trabecular bone architecture on 2D planar sections. Whitehouse defined the 'mean intercept length' (MIL) at some arbitrarily chosen direction as the relative bone area divided by the total projected boundary perimeter per unit area. When MIL data is plotted as a radius from the origin at the angle of measurement, a curve remarkably close to an ellipse is generated. A departure from isotropy is characterized by the ratio of the ellipse semi-axes. Harrigan and Mann (1984) extended this concept to 3D by taking MIL measurements on three mutually perpendicular planes of cubic bone specimens and introduced a tensor-valued measure of bone architecture called the 'mean intercept length tensor'. With the advent of 3D imaging techniques such as microcomputed tomography (μCT) (Sasov, 1987; Sasov and Van Dyck, 1998) and high resolution magnetic resonance imaging (MRI) (Chung et al., 1995), the fabric of a bone sample may be readily detected without resorting to model-based approaches (e.g., Odgaard et al., 1990) or extrapolating 3D information from a restricted set of 2D images (e.g., Harrigan and Mann, 1984; Kanatani, 1985a).

The main component of this paper is the identification and quantification of the fabric of porous materials. Directionally dependent measurements are obtained by probing binarized μCT images with arrays of parallel test lines. In Section 2, several currently used measures of fabric are defined and a new fabric descriptor referred to as *areal pore size distribution* is introduced. Subsequently, a brief discussion of the mathematical representation of directional data is provided based on the work of Kanatani (1984) and extended in light of recent developments by Pietruszczak and Mroz (2001). In Section 3, algorithms for the identification of various measures of fabric are described in a pseudocode. A simple and efficient computational scheme, known as the *generalized spiral points method* (Saff and Kuijlaars, 1997) is employed for the generation of isotropically and uniformly distributed test probes. Section 4 addresses the problems of quantification, interpretation and visual presentation of microstructural information within the context of a practical example: fabric analysis of trabecular bone images. In particular, the performance of different fabric descriptors is examined and the results compared in terms of specification of eigenvalues and the degree of anisotropy.

2. Fabric descriptors for porous materials

The standard procedures based on stereology incorporate unbiased test probes to estimate structural parameters. Both high and low order dimensional probes, such as points, lines and planes, can be used to measure various quantities of interest, including length, surface area, volume, etc. Lineal probes are particularly well suited for deriving orientation dependent information since they can be counted, incorporate the additional components of direction and length, and are simple to manipulate geometrically. For this reason, those descriptors which rely on parallel arrays of lineal probes have been included in this work.

In general, each fabric descriptor is based on sums and numbers of lineal intercept quantities. The probes are usually equally spaced and are rotated from a standard alignment configuration into a prescribed sampling direction v_i. Consider the following basic measurement quantities derived from an array of parallel test lines. Let $L(v_i)$ be the total length of test lines. Depending on the surface representation of the volume of interest, $L(v_i)$ may be constant (i.e., sphere) or orientation-dependent (i.e., prism, cylinder). An intercept is an isolated line segment arising from the intersection of a test line with the boundary of the phase of interest and lying within this phase. Then $\sum I(v_i)$ represents the sum of all intercept lengths while $N(v_i)$ corresponds to their number.

In this paper the performance of some fabric measures currently used in the area of biomechanics (cf. Odgaard, 1997a) is assessed. The descriptors included in the evaluation process are listed below.

- *Mean intercept length* (MIL) was originally introduced in the article by Whitehouse (1974), in which a formula was proposed for calculating the mean width of trabeculae as seen in 2D scanning electron microscope micrographs. The definition in a 3D context may be expressed as

$$\mathrm{MIL}(v_i) = \mu_{\mathrm{v}}(v_i)\frac{L(v_i)}{N(v_i)} = \left(\frac{\sum I(v_i)}{L(v_i)}\right)\left(\frac{L(v_i)}{N(v_i)}\right) = \frac{\sum I(v_i)}{N(v_i)} \tag{1}$$

  where μ_{v} is the lineal fraction of voids in the direction v_i. It is noted that μ_{v} is an orientation independent quantity, so that the effect of anisotropy is embedded in the second term, L/N. Thus, μ_{v} can in fact be excluded from definition (1) (cf. Odgaard, 1997a). The reason for retaining this parameter here is two-fold. First, the mechanical characteristics of porous media are strongly affected by the volume fraction of voids, so that the information regarding this quantity is, in general, very useful. Second, the representation employing $\sum I$ is convenient as all the other measures discussed below are defined in terms of the same fundamental quantity.
- *Star length distribution* (SLD) was introduced by Smit et al. (1998), who presented a volume-based method for the quantification of anisotropy in porous media. SLD defines the mean length of an object in a given direction at a random material point. The definition using lineal probes is

$$\mathrm{SLD}(v_i) = \frac{\sum I^2(v_i)}{\sum I(v_i)} \tag{2}$$

  In the above formula, the intercepts are weighted by their length. As a result, the measurements of SLD are more sensitive to the detection of microstructural orientation than those involving MIL.
- *Star volume distribution* (SVD) was originally proposed by Cruz-Orive et al. (1992) and is conceptually related to the *volume orientation* descriptor (VO) introduced by Odgaard et al. (1990). This measure is similar to SLD with the exception that intercepts are weighted more heavily. A point grid algorithm for calculating SVD was recently presented by Odgaard et al. (1997b). Here, a regularly spaced point grid is generated over the sampling domain. The subset of points that fall within the phase of interest is retained for scanning. For each member of a set of uniformly distributed orientations, a test line is generated at every sampling point and an intersection with the phase of interest is determined. Averaging the cubed intercept lengths over all of the points yields the mean volume as a function of orientation. In this case, the definition of SVD becomes

$$\mathrm{SVD}(v_i) = \frac{\pi}{3}\frac{1}{M}\sum_{k=1}^{\mathrm{M}} I_k^3(v_i) \tag{3}$$

  where M specifies the number of test points. Alternatively, SVD can be calculated using an array of parallel test lines (Smit et al., 1998) according to

$$\mathrm{SVD}(v_i) = \frac{\pi}{3}\frac{\sum I^4(v_i)}{\sum I(v_i)} \tag{4}$$

A new fabric measure proposed here is referred to as *areal pore size distribution* (APS). To define this measure, a representative volume of the material is considered in the form of a spherical sampling domain of radius R. A Cartesian coordinate system is then fixed at the centroid of this sphere. The identification process involves cutting the sphere with a plane of unit normal v_i and placing on it a set of uniformly distributed parallel lines aligned in an arbitrary direction, ω_i, so that v_i is orthogonal to ω_i. The areal "pore size" is then defined as

$$\rho_{\mathrm{A}}(v_i) = \frac{1}{2\pi}\int_{C(v_i)} g(\omega_i)\,\mathrm{d}C; \quad g(\omega_i) = \frac{\sum I(\omega_i)}{N(\omega_i)} \tag{5}$$

where dC is the differential angle measured in this plane and $g(\omega_i)$ is symmetric with respect to the origin; i.e., $g(\omega_i) = g(-\omega_i)$. The APS descriptor is now obtained by averaging ρ_A along the direction v_i, i.e.,

$$\mathrm{APS}(v_i) = \frac{1}{2R}\int_{-R}^{R} \rho_A(v_i)\,dL \tag{6}$$

where dL is the differential distance measured along v_i.

In the implementation of a line algorithm, the integration is replaced by a discrete summation. Consider a set of equally spaced, parallel test lines on any one of a set of M equally spaced, parallel planes. The test lines are rotated in-plane k times around a pole defined by v_i. Thus, in terms of the discrete quantities I and N:

$$APS(v_i) = \frac{1}{M}\sum_{j=1}^{\mathrm{M}} \rho_A^{(\mathrm{j})}(v_i); \quad \rho_A^{(\mathrm{j})}(v_i) = \frac{1}{k}\sum_{k} \frac{\sum I(\omega_i^{(\mathrm{k})})}{N(\omega_i^{(\mathrm{k})})}; \quad \omega_i^{(\mathrm{k})} \cdot v_i = 0 \tag{7}$$

In order to increase the accuracy of the numerical integration, viz. Eq. (7), it is convenient to assume that the test line density remains constant for all M planes. Therefore, in the case of a spherical sampling domain, the test line spacing within each planar disc perpendicular to the sampling direction is different. The closest spacing between test lines occurs on discs near the poles, whereas the farthest spacing occurs at the equatorial plane.

The above fabric measure is particularly convenient for describing the hydraulic properties of porous media (e.g., permeability characteristics). It should be emphasized that a detailed geometric representation of the pore space is impossible and the APS descriptor is introduced here in a statistical sense. The areal "pore size" ρ_A is defined herein as an in-plane orientation average of $g(\omega_i)$ which, in turn, represents the ratio of the area of voids to the projected boundary perimeter. Such a measure may be implemented in the context of a network model of porous structure, whereby the pore space is visualized as an arrangement of capillary tubes whose diameter vary according to the spatial distribution of the APS descriptor. In this way, an explicit correlation between the hydraulic conductivity tensor and that derived on the basis of APS measurements may be established.

In general, the fabric descriptors listed here, i.e., MIL, SLD and SVD, have been chosen on a rather selective basis. Several other measures, such as *mean free path* (Underwood, 1970), *areal porosity distribution* (Pietruszczak et al., 1999), etc., have also been used in the area of biomechanics. In addition, other measures of microstructure have been developed in the field of geomechanics, which include the distribution of interparticle contacts (Oda, 1972), distribution of microcracks in brittle materials (Kanatani, 1985b), etc. As mentioned earlier, a comprehensive review of existing measures is not a primary objective here. The focus of this work is on the algorithmic aspects of the identification procedure, which can be adequately illustrated in the context of the descriptors presented above.

Given the definitions of fabric descriptors, Eqs. (1)–(7), an important issue now is that of the mathematical representation of the distribution of fabric data. In general, the distribution function may be assumed in the form suggested by Kanatani (1984)

$$f(v_i) = C(1 + D_{ij}v_iv_j + D_{ijkl}v_iv_jv_kv_l + \cdots) \tag{8}$$

where C represents the mean value of the descriptor while D's are symmetric, traceless even ranked tensors which describe the directional variation or deviation from the mean. The simplest approximation to Eq. (8) is that in which only the second-order tensor is retained, i.e.,

$$f(v_i) = C(1 + D_{ij}v_iv_j); \quad D_{kk} = 0; \quad D_{ij} = D_{ji}; \quad v_kv_k = 1 \tag{9}$$

An alternative to this formulation is

$$f(v_i) = 3CA_{ij}v_iv_j; \quad A_{kk} = 1; \quad A_{ij} = A_{ji} \tag{10}$$

where A_{ij}, which may be referred to as a normalized 'fabric tensor', is defined as

$$A_{ij} = \frac{1}{3}(\delta_{ij} + D_{ij}) \tag{11}$$

For a smooth orthogonal anisotropy, it is sufficient to retain the representation (9) or (10). The interpretation is that D_{ij} vanishes for an isotropic distribution. For non-zero D_{ij}, the eigenvectors, $e_i^{(k)}$, define the symmetry axes while the corresponding eigenvalues, λ_k, are the ratios of the distribution to the isotropic distribution along these axes, i.e.,

$$f\left(e_i^{(k)}\right) = C(1+\lambda_k) \Rightarrow \frac{f\left(e_i^{(k)}\right)}{C} \propto \lambda_k \tag{12}$$

In geometric terms, the principal values of D_{ij} define the semi-axes of an ellipsoidal shape. If D_{ij} vanishes, the distribution function, plotted as a radial vector, defines a sphere with radius C.

The distribution function retaining the fourth-order tensor has the form

$$\begin{aligned} &f(v_i) = C(1 + D_{ij}v_iv_j + D_{ijkl}v_iv_jv_kv_l) \\ &D_{kk} = 0; \quad D_{ij} = D_{ji}; \quad v_kv_k = 1, \\ &D_{ijkl} = D_{jikl} = D_{klij} = D_{lkij}; \quad D_{ijij} = 0 \end{aligned} \tag{13}$$

With this approximation, higher material symmetries are possible, as noted by Zysset and Curnier (1995).

Most naturally occurring as well as manufactured porous materials exhibit either transverse isotropy (e.g., sedimentary rocks, soils, cortical bone, etc.) or, in some instances, orthotropy (e.g., structural masonry, trabecular bone). Therefore, representation (9) may, in general, be adequate. However, in order to attain a higher degree of accuracy in fitting measurement data, the approximation (9) can be extended by incorporating dyadic products of the second-order tensor (Pietruszczak and Mroz, 2001). In this case the modified nth-order form is

$$\begin{aligned} f(v_i) &= C_0(1 + D_{ij}v_iv_j + C_1(D_{ij}v_iv_j)^2 + \cdots + C_{n-1}(D_{ij}v_iv_j)^n) \\ &= C_0\left(1 + D_{ij}v_iv_j + \sum_{k=2}^{n} C_{k-1}(D_{ij}v_iv_j)^k\right) \end{aligned} \tag{14}$$

The main advantages of this representation are that orthotropic symmetry is retained, a simple geometric interpretation is preserved, and the implementation within a mechanical framework is less complex. It should be noted that, in the expression above, the constant C_0 represents the value of $f(v_i)$ in the direction of the space diagonal, i.e., $v_i = \{1,1,1\}/\sqrt{3}$, and it does not, in general, correspond to the mean value.

3. On identification of fabric measures from μCT images

The goal of this section is to outline two algorithms that compute the three basic quantities: $N(v_i)$, $\sum I(v_i)$ and $L(v_i)$, from which various descriptor measurements are calculated. The first algorithm is based on an isotropic line array definition and generates MIL (Eq. (1)), SLD (Eq. (2)) and SVD (Eq. (4)) measurements. The second algorithm is based on a non-uniform line array specification and provides APS (Eq. (7)) measurements.

The basic procedure in both cases begins with a specification of the geometry of the sampling domain, or volume of interest (VOI), symbolized by Ω_S (e.g., a sphere, cylinder, or prism). A 'global' control volume, Ω_G, is then generated which is the circumsphere that encloses Ω_S. Next, a set of points is defined on the equatorial plane of Ω_G in a manner that depends on whether a uniform or non-uniform sampling grid is

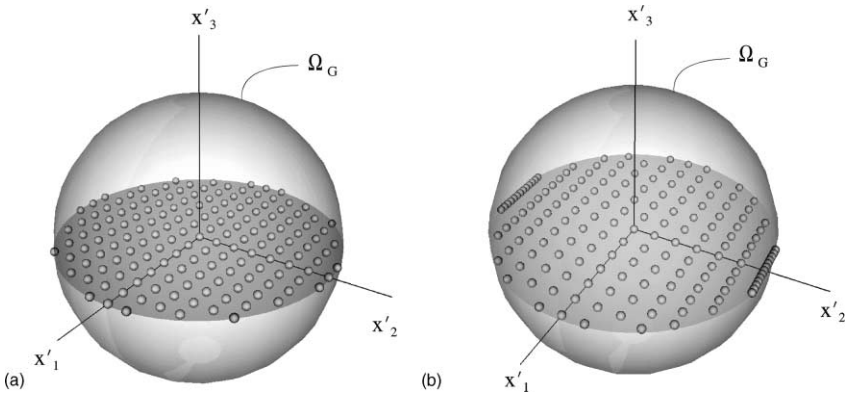

Fig. 1. Regularly (a) and irregularly (b) spaced grid points (test lines not shown).

required. In the case of the former, the points define an array of isotropically spaced, parallel test lines. In the case of a non-uniform grid, a set of equally spaced parallel planes with unit normal v_i is defined such that the test line density increases on planes nearer to the poles of Ω_G. Fig. 1 shows examples of both uniform and non-uniform grids.

For each sampling orientation, the line segments arising from the intersection of the test lines with Ω_S are scanned in a discrete manner to derive the basic descriptor quantities. To scan along a test line segment, a voxel marching scheme is employed (see, for example, Cohen, 1994). Given the starting position p_i^0 of a line segment on the boundary of Ω_S and the sampling orientation, the test line is scanned incrementally and consecutive voxels are stored (i.e., position and phase classification) until the end point on the boundary is reached

$$p_i^k = \text{round}(p_i^0 + k\bar{v}_i) \wedge p_i^k \in \Omega_S; \quad \bar{v}_i = v_i / \max(\{|v_1|, |v_2|, |v_3|\}) \tag{15}$$

The 'round' function converts Cartesian coordinates of the kth voxel to integer indices. Once identified, this temporary set of voxels, say Q, is scanned for intercepts.

A heuristic procedure known as *pattern matching* has been developed to minimize errors in intercept identification that arise from the discrete representation of both the test lines and the surface of the phase of interest within an image (cf. Kuo and Carter, 1991). A pair of kernels, each containing three classification elements, is superimposed over the data set Q to identify the origins and terminations of intercepts. Fig. 2a and 2b show the location of intercepts using this approach while Fig. 2c shows the rejection of a false intercept. Here, a *one* classifies a member of the phase of interest. An intercept length is defined as the midpoint location between voxels wherein a phase transition occurs. Once complete, sums of intercept quantities are updated for further processing.

The intercept identification and storage process is performed for all test line segments under a given alignment configuration. Descriptor measurements are calculated from ratios of the sums of basic intercept quantities and are then archived for post-processing. The set of test line segments is redefined for each alignment configuration.

Figs. 3 and 4 present a pseudocode description of the uniform and non-uniform line array algorithms, respectively. Here, a capital letter signifies a set of unique scalar elements while a bolded capital letter identifies a set of vectors. $\emptyset$ corresponds to the empty set and is used to initialize a set of elements. The union symbol, '$\cup$', serves as an operator to add elements to a given set. The '$\leftarrow$' notation assigns a left-hand side variable the result of a right-hand side expression. A capital N with a subscript corresponding to a set identifier means 'number of elements in' the set. Given the preceding definitions:

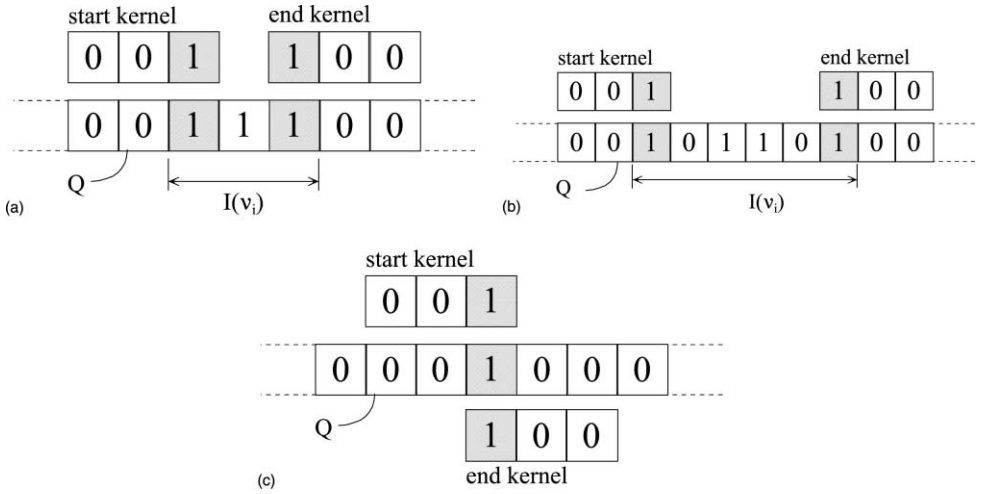

Fig. 2. Pattern matching examples: identification of intercepts (a), (b) and detection of a false intercept or spur i.e., $I = 0$ (c).

form uniform set of grid points, $\boldsymbol{X}$, *in* $\boldsymbol{x}$ *reference frame*
project $\boldsymbol{X}$ *onto* Ω_G
$MIL \leftarrow SLD \leftarrow SVD \leftarrow \varnothing$
for $(i = 1, 2, \ldots, N_\Theta)$ ***do***
  transform $\boldsymbol{X}$ *to* $\boldsymbol{X}'$ *in* $\boldsymbol{x}'$ *reference frame*
  form set of test line segments that intersect Ω_S, $\boldsymbol{T}$, *from* $\boldsymbol{X}'$
  $s_4 \leftarrow s_3 \leftarrow s_2 \leftarrow s_1 \leftarrow 0$
  for $(j = 1, 2, \ldots, N_T)$ ***do***
    form $1D$ *contiguous set of voxels*, $\boldsymbol{Q}$, *by incrementing along current test line*
    extract set of intercepts, $\boldsymbol{I}$, *from* $\boldsymbol{Q}$ *using pattern matching paradigm*
    $s_1 \leftarrow s_1 + \sum I$
    $s_2 \leftarrow s_2 + \sum I^2$
    $s_3 \leftarrow s_3 + \sum I^3$
    $s_4 \leftarrow s_4 + N_I$
  end do
  $MIL \leftarrow MIL \cup \{s_1/s_4\}$
  $SLD \leftarrow SLD \cup \{s_2/s_1\}$
  $SVD \leftarrow SVD \cup \{\frac{\pi}{3} s_3/s_1\}$
end do

Fig. 3. A uniform line array algorithm to generate MIL, SLD and SVD measurements.

- $S \leftarrow \emptyset$ means initialize the set of scalars, S, to the empty set.
- $s_2 \leftarrow s_1 \leftarrow 0$ is a compound assignment statement initializing the scalars s_1 and s_2 to zero.
- $S \leftarrow S \cup \{s_1, s_2\}$ means add elements s_1 and s_2 to set S.
- N_S is the number of elements in the set S.

```
form non-uniform sets of grid points, X_j, in x reference frame
project all X_j onto Ω_G
APS ← ∅
for (i = 1, 2, ..., N_Θ) do
  S ← ∅
  for (j = 1, 2, ..., N_X) do
    s ← 0
    for (k = 1, 2, ..., N_Ψ) do
      transform X_j to X'_j in x' reference frame
      form set of test line segments that intersect Ω_S, T, from X'_j
      for (l = 1, 2, ..., N_T) do
        form 1D contiguous set of voxels, Q, by incrementing along current test line
        extract set of intercepts, I, from Q using pattern matching paradigm
        s ← s + ∑ I/N_I
      end do
    end do
    S ← S ∪ {s/N_Ψ}
  end do
  APS ← APS ∪ {∑ S/N_S}
end do
```

Fig. 4. A nonuniform line array algorithm to generate APS measurements.

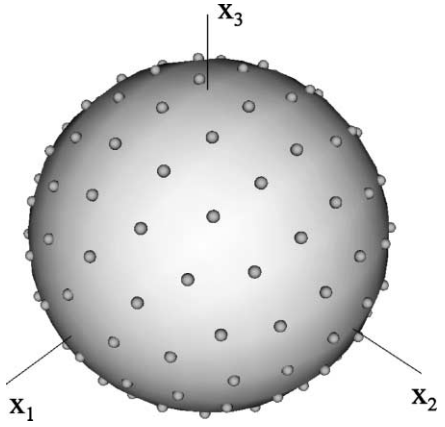

Fig. 5. 150 spiral points on a unit sphere.

Since the primary objective of the algorithms is to obtain a distribution of quantities being measured, or of quantities derived from them, the sampling orientations themselves are of no particular interest and should not influence the results. However, a uniform distribution of sampling directions is required for obtaining a set of descriptor measurements that will be subjected to the application of a least squares fitting procedure. The generation of a sequence of uniformly distributed directions in 3D, or points on a unit sphere, is non-trivial and in general, problem specific. The notion of uniformity can be realized, for example, by sampling with a number of random orientations. However, it is desirable to incorporate a computationally efficient and reproducible scheme, as in the manner of certain quadrature formulae, yet

without restriction on the number of sample points. In this paper, a simple, explicit construction scheme known as the '*generalized spiral points method*' has been adopted. The method is straightforward to implement and places no restriction on the number of points. The reader is referred to Rakhmanov et al. (1994) for theoretical details and to Saff and Kuijlaars (1997) for the specifics of the implementation. As an example, Fig. 5 shows the distribution of 150 points on the unit sphere obtained using this approach.

Finally, it should be mentioned that the accuracy of the algorithms described in this section has been tested in the context of simple structures composed of a spherical/ellipsoidal inclusion embedded within a larger sampling domain. For all descriptors considered here, i.e., MIL, SLD, SVD and APS, the results were consistent with the closed-form solutions, which can easily be established for these elementary geometric entities (cf. Smit et al., 1998).

4. Fabric analysis for trabecular bone images

Two μCT images of cylindrical bone biopsies from the femoral neck were obtained in binarized form from Dr. Ralph Mueller (Orthopaedic Biomechanics Laboratory, Beth Israel Deaconess Medical Center). Table 1 summarizes the general image characteristics. The abbreviations BVF and DA refer to the bone volume fraction ($\mathrm{BVF} = 1 - \hat{\mu}_{\mathrm{V}}$) and the degree of anisotropy, respectively. Here, the degree of anisotropy is defined as the ratio of the maximum to minimum MIL eigenvalue, where the MIL tensor is defined as in Harrigan and Mann (1984).

For the purpose of verification, the values of BVF and DA, as provided by Dr. Mueller, were reassessed using the procedure outlined in Fig. 3. In particular, the MIL measurements were obtained with the uniform line array algorithm using a spherical VOI with $R_{\mathrm{G}} = 135$ voxels, a grid spacing of 10 voxels, and the pattern matching algorithm turned off. BVF was determined via a direct voxel counting algorithm within the same spherical volume. The results (in brackets) are in reasonable agreement with the original values provided in Table 1.

Figs. 6 and 7 show the boundary projection of the spherical volume of interest overlaid on three average intensity projection images of the femur_1 and femur_2 samples, respectively. The corresponding volume renderings were generated by ray casting along the direction normal to the plane starting at the center of the VOI. These images clearly illustrate that for similar porosity values, the underlying structural arrangement of trabeculae can be significantly different. The femur_1 sample consists of a heterogeneous arrangement of both rod and small plate structures while the femur_2 sample exhibits larger plate structures with fewer rods.

To select a suitable grid spacing, both images were subjected to a series of preliminary scans to determine the mean BVF relative percent error over a range of grid spacings. The true BVF is determined by counting the number of phase of interest voxels and dividing by the total number of voxels contained within the VOI. The line grid algorithm was used to scan the images with 50 spiral points, pattern matching turned off and grid spacings of $\delta = \{5, 10, 15, \ldots, 30\}$ voxels. Fig. 8 shows the mean relative percent error in BVF

Table 1
General image characteristics

Identification	Femur_1	Femur_2
BVF	18% (17.7%)	18% (17.5%)
DA	1.25 (1.26)	1.47 (1.52)
Image dimensions	$336 \times 336 \times 310$	
Voxel size (isotropic)	28 μm	
Sample dimensions	Diameter ~8.3 mm, height ~8.7 mm	

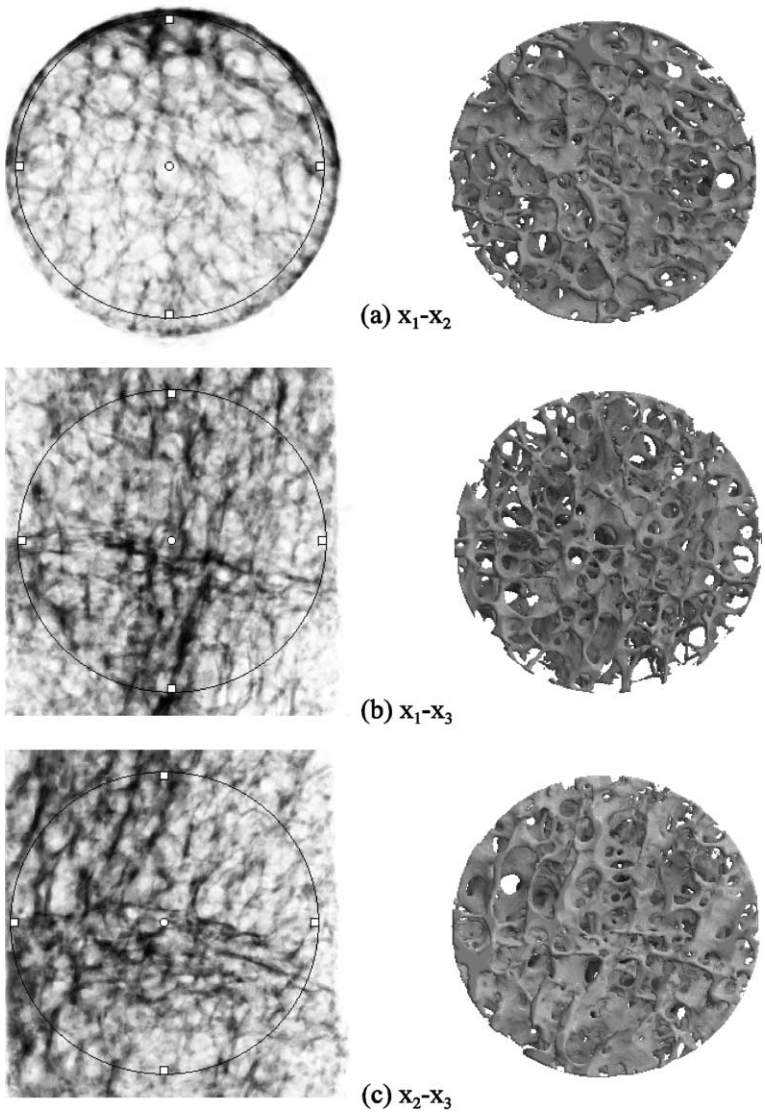

Fig. 6. VOI overlaid on three average intensity projection images of femur_1.

over the range of grid spacings for both images. Based on these results, a grid spacing of 10 voxels was adopted for all of the subsequent descriptor measurements.

In what follows, the results of the analysis of the femur_1 image are presented using the fabric descriptors identified in Section 2. In all cases, 100 spiral points were used to scan the solid (bone) phase. The measurement data was fit to Eq. (14) with orders of fit $n \in \{1, 2, \ldots, 5\}$, using an iteratively re-weighted least squares procedure (e.g., Myers, 1990) combined with a Levenberg–Marquardt solution scheme for the case when $n > 1$. For each descriptor, the χ^2 merit function was evaluated. Values were subsequently normalized with respect to the maximum χ^2 value, usually obtained with $n = 1$, for comparative evaluations.

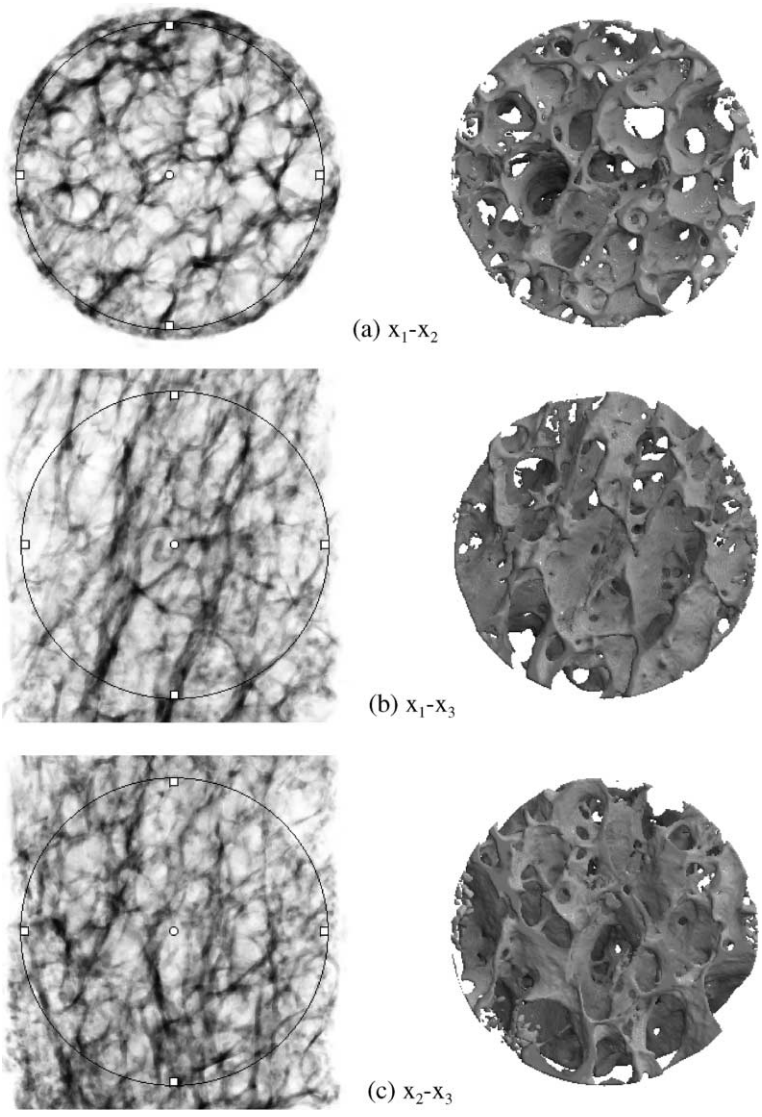

Fig. 7. VOI overlaid on three average intensity projection images of femur_2.

Fig. 9 presents plots of order of fit versus normalized χ^2 for each descriptor. Series distinguished by 'pm on' or 'pm off' refer to measurements obtained with and without pattern matching, respectively. For most descriptors, increasing the order of fit beyond two does not lead to a substantial improvement in the fit itself. In the case of MIL, pattern matching significantly affects the measurement distribution and in turn the required order of fit to capture fluctuations in the data. On the other hand, for APS, pattern matching has less of an influence on the distribution of data (primarily due to the averaging of measurements around the main sampling direction), and the improvement in fit is not significant for higher order approximations.

Fig. 10 presents a series of best fit approximations, based on Eq. (14), versus measured values of SLD. The first and second-order distribution functions have been evaluated in 10° increments within each of the three principal material planes. It should be noted that the orientations associated with the discrete

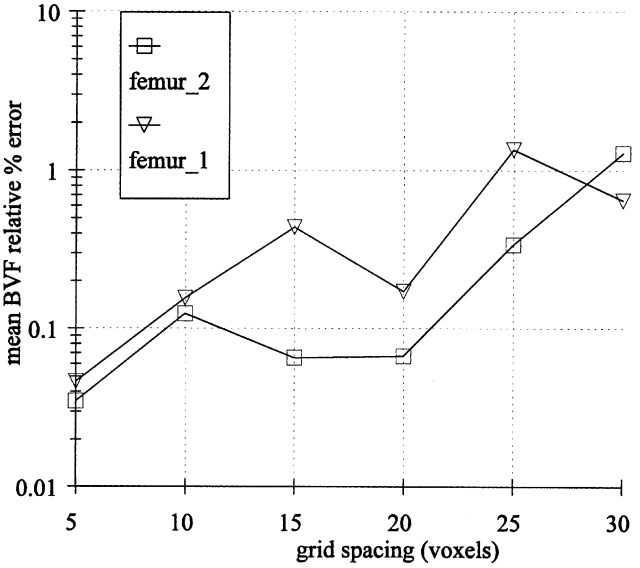

Fig. 8. Grid spacing versus mean relative percent error in BVF for femur_1 and femur_2 images.

measurement points are not the same for $n = 1$ and $n = 2$, since the detected principal triad changes slightly for different orders of fit. It is evident from Fig. 10 that a noticeable improvement in fit is obtained for $n = 2$. In Fig. 11, similar results are presented for SVD. Here, it is apparent that there is a considerable amount of fluctuation in the measurements, so that a higher order fit is necessary to capture the general trends in the distribution of data.

To provide a geometric representation of different fabric descriptors, a visualization scheme advocated by Westin et al. (1999) has been adopted. According to this approach, a symmetric second-order tensor can be represented as an object which is a combination of a line, a disk and a sphere. The line segment describes the major principal direction of the tensor and its length is proportional to the largest eigenvalue. The disk describes the plane spanned by the eigenvectors corresponding to the two largest eigenvalues. The sphere has a radius proportional to the smallest eigenvalue.

The tensor A_{ij}, Eq. (11), can be decomposed into a sum of components in the tensor basis which is a combination of the dyadic products of the principal triad

$$A_{ij} = (\lambda_1 - \lambda_2)A^{\mathrm{l}}_{ij} + (\lambda_2 - \lambda_3)A^{\mathrm{p}}_{ij} + \lambda_3 A^{\mathrm{s}}_{ij} \tag{16}$$

where

$$A^{\mathrm{l}}_{ij} = e^{(1)}_i e^{(1)}_j; \quad A^{\mathrm{p}}_{ij} = e^{(1)}_i e^{(1)}_j + e^{(2)}_i e^{(2)}_j; \quad A^{\mathrm{s}}_{ij} = e^{(1)}_i e^{(1)}_j + e^{(2)}_i e^{(2)}_j + e^{(3)}_i e^{(3)}_j \tag{17}$$

where e_i's and λ's are the eigenvectors and eigenvalues of A_{ij}, respectively, and the superscripts l, p and s stand for 'line', 'plane' and 'sphere', respectively.

A normalized set of tensor basis coordinates can be defined as:

$$\begin{aligned} &c_{\mathrm{l}} = \frac{\lambda_1 - \lambda_2}{\lambda_1}; \quad c_{\mathrm{p}} = \frac{\lambda_2 - \lambda_3}{\lambda_1}; \quad c_{\mathrm{s}} = \frac{\lambda_3}{\lambda_1} \\ &c_{\mathrm{l}} + c_{\mathrm{p}} + c_{\mathrm{s}} = 1 \wedge |\lambda_1| \geqslant |\lambda_2| \geqslant |\lambda_3| \end{aligned} \tag{18}$$

so that the degree of ansiotropy can be measured as the deviation from the spherical (isotropic) case;

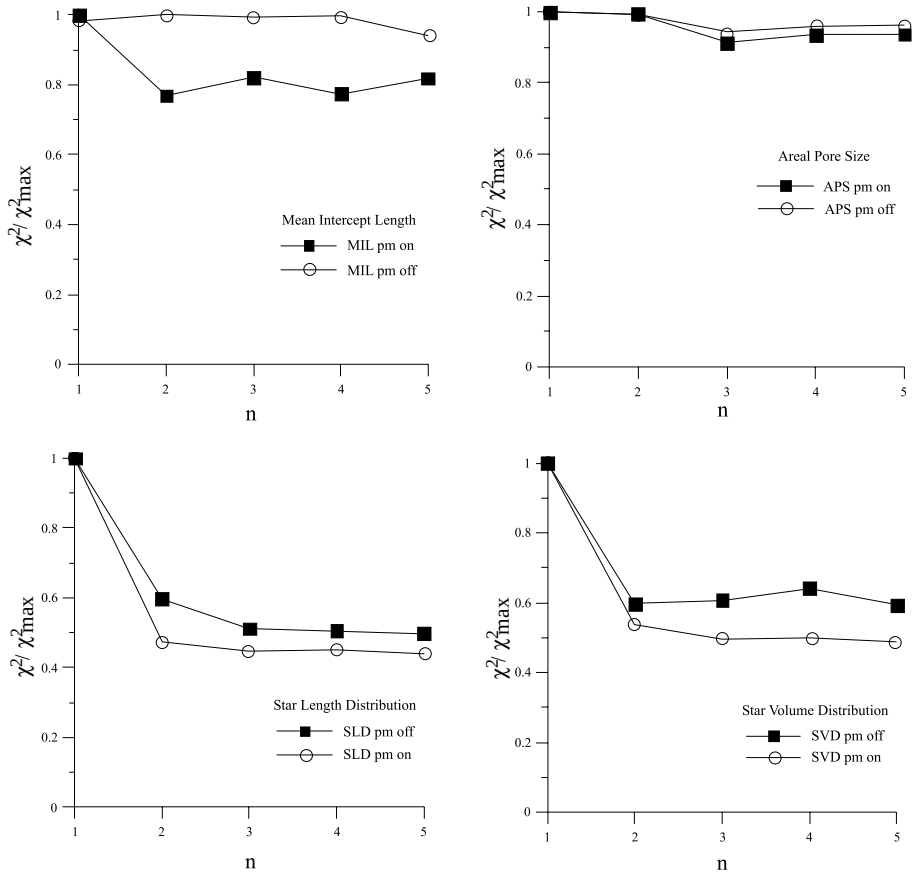

Fig. 9. Order of fit, n, versus normalized χ^2 for various fabric descriptors; femur_1 image.

$$DA = 1 - c_s = 1 - \frac{\lambda_3}{\lambda_1} \tag{19}$$

with magnitude dependent upon the descriptor.

An additional series of plots of order of fit versus the tensor basis coordinates c_s, c_p and c_l, is presented in Fig. 12 for the line array descriptors evaluated with pattern matching on. For orders of fit greater than one the response is generally smooth, indicating that a second-order fit sufficiently captures the anisotropy information. The sample is strongly anisotropic if evaluated by SVD, while a weaker form of anisotropy is detected by APS, MIL and SLD descriptors. It should be noted that interpretation of the anisotropy information by means of tensor basis coordinates (i.e., Eq. (18)) or by DA (i.e., Eq. (19)) is only tentative in nature. The correlation with mechanical properties remains to be ascertained by a comprehensive experimental investigation, which is beyond the scope of the present research.

Fig. 13 presents the geometric representation of the respective fabric descriptors. Here, the three component objects are plotted as ellipsoids with semi-axes scaled to a maximum of 1. Thus, the length of the line segment is 1, the radius of the disk is λ_2/λ_1, whereas the radius is the sphere is λ_3/λ_1. Surface shading has been employed to enhance the contrast between geometric entities. The composite shapes provide an immediate visual interpretation of the underlying symmetry via the relative magnitudes of the normalized principal descriptor values. Principal fabric triads and the orientation of the image frame of reference are

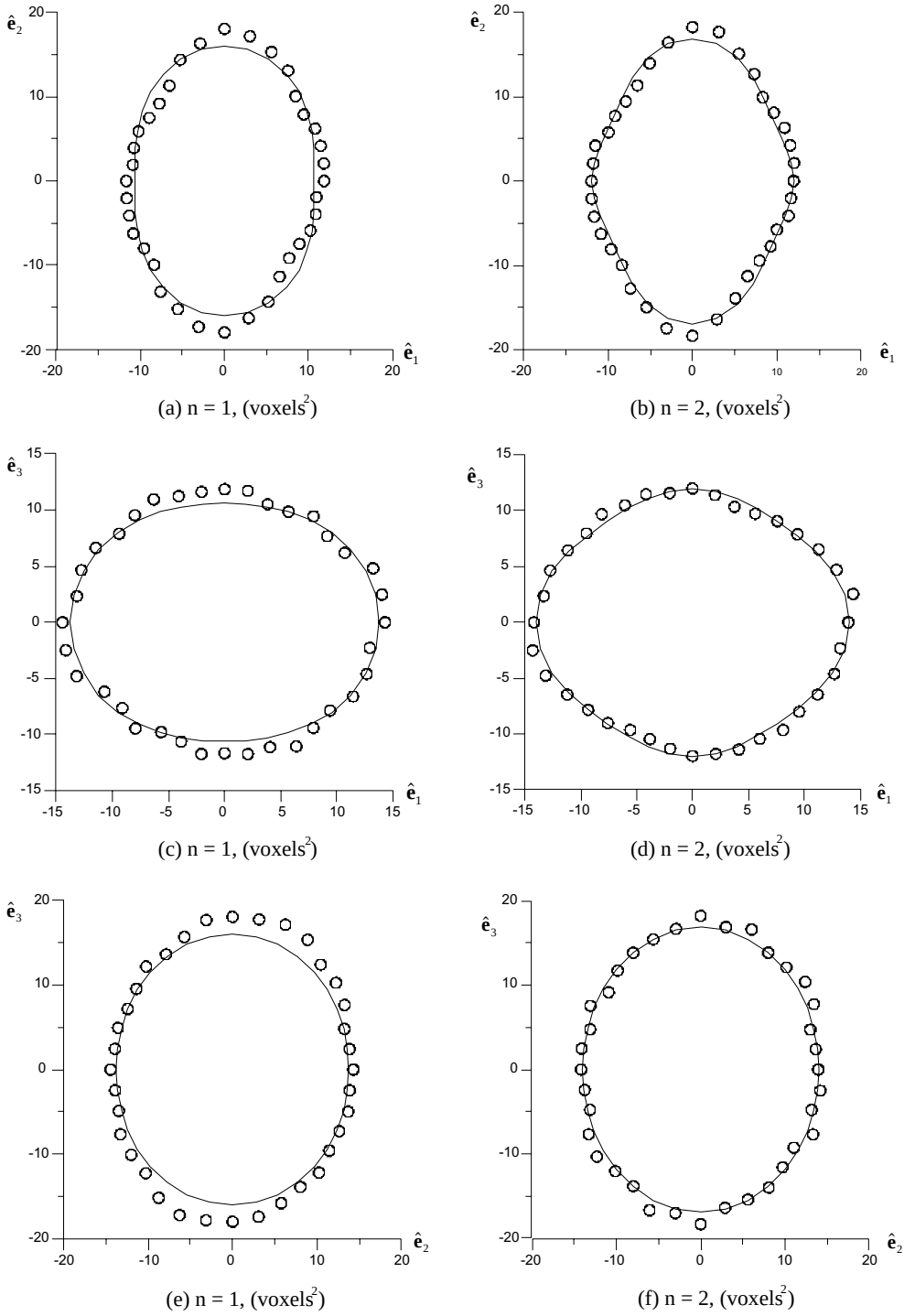

Fig. 10. Best fit approximations '–' versus measured values '○' of SLD; femur_1 image, principal plane view.

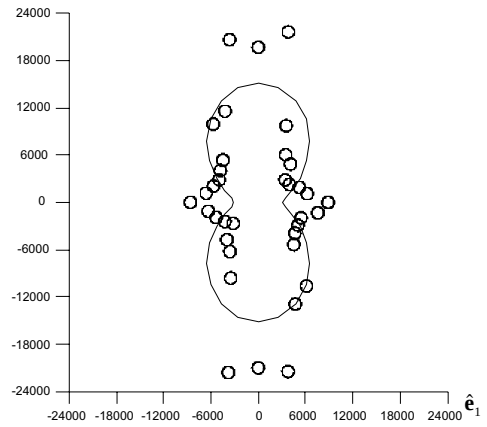

(a) n = 1, (voxels^3)

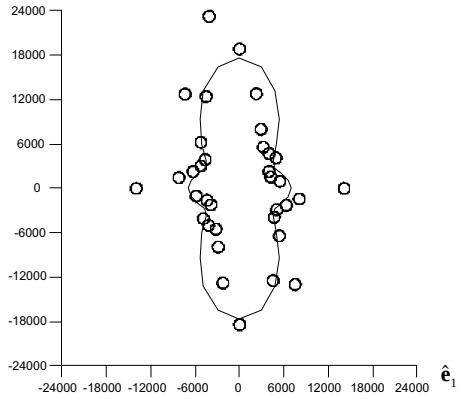

(b) n = 2, (voxels^3)

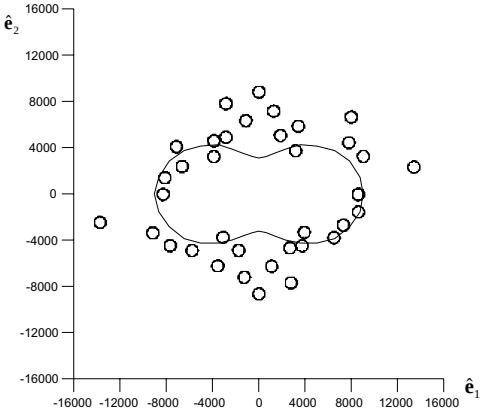

(c) n = 1, (voxels^3)

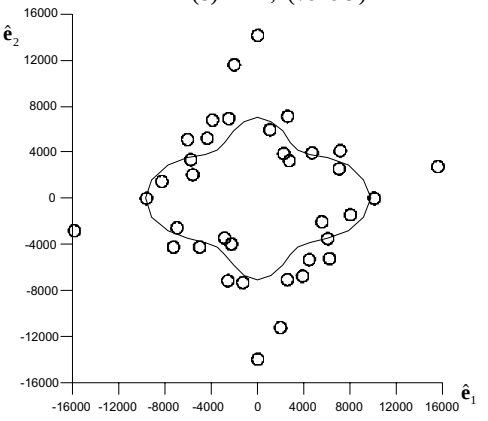

(d) n = 2, (voxels^3)

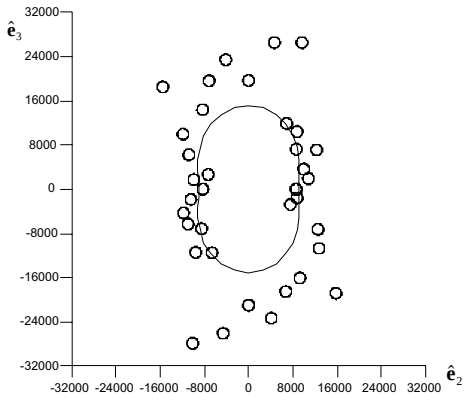

(e) n = 1, (voxels^3)

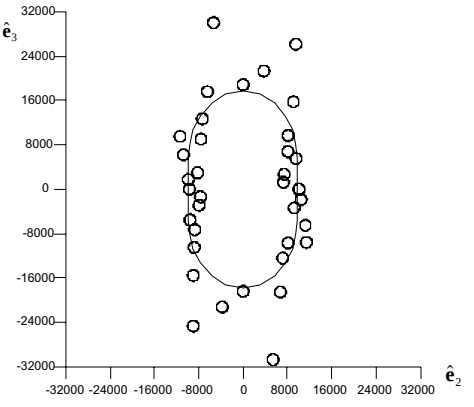

(f) n = 2, (voxels^3)

Fig. 11. Best fit approximations '–' versus measured values 'o' of SVD; femur_1 image, principal plane view.

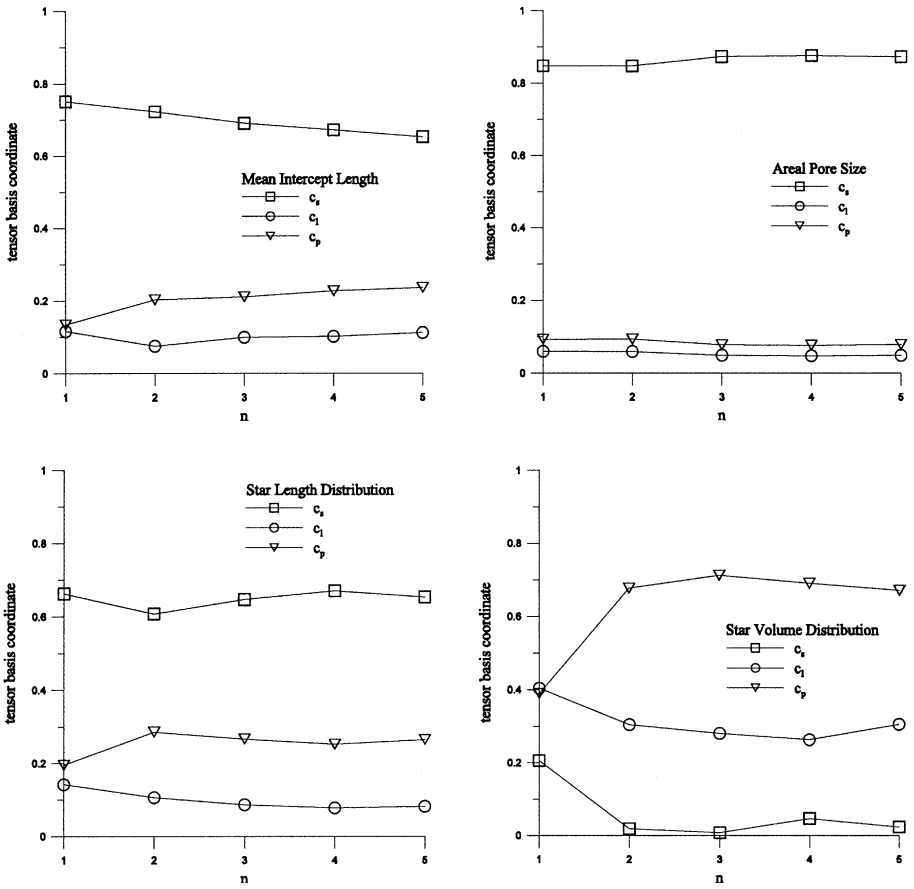

Fig. 12. Order of fit, n, versus tensor basis coordinates for various fabric descriptors; femur_1 image.

also shown. The symmetry characterization is visually apparent with SVD displaying a strong anisotropy, as indicated by the absence of a spherical component, while the other descriptors indicate varying degrees of anisotropy.

A comparison of principal material triads in Fig. 13 reveals that MIL, SLD and SVD detect approximately the same orientation while APS, due to its definition, presents a similar configuration but in a different order; i.e., direction 3 is the same as direction 1 identified by the other descriptors.

The sensitivity of orientation detection to the order of fit is examined in Fig. 14. Here, the principal fabric orientations are plotted in angular coordinates, θ and φ, for different orders of fit relative to the image frame of reference. The plots reveal that the detection of orientation is relatively stable for $n > 1$, which is consistent with the results shown in Fig. 12.

The subsequent Figs. 15–17 present the results for the femur_2 image. All descriptors were identified using the line array algorithms with the following initial parameters: 100 spiral points, $\delta = 10$ voxels and the pattern matching algorithm employed.

Trends in order of fit versus normalized χ^2 were similar to those observed for the femur_1 image (Fig. 8) and, therefore, are not presented here. Fig. 15a–d show the tensor basis coordinates, c_l, c_p and c_s, versus order of fit for the various descriptors. The APS and MIL descriptors (Fig. 15a and b) provide a smooth

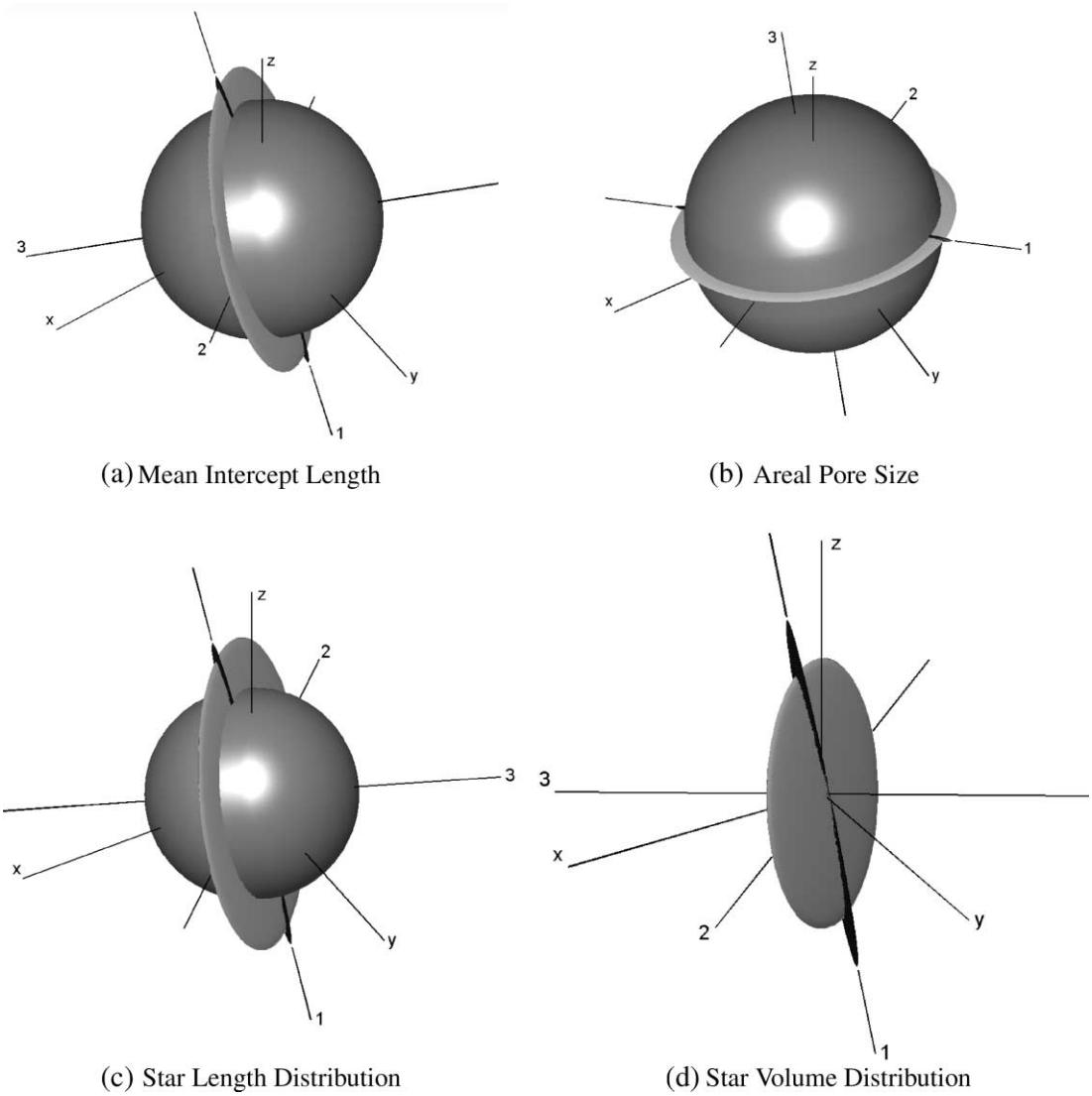

Fig. 13. Geometric representation of different fabric descriptors; femur_1 image, $n = 2$.

response for $n > 1$, indicating that a second-order fit is sufficient. A relatively stable response is obtained with $n > 2$ in the case of SLD (Fig. 15c), with the exception of the data corresponding to $n = 4$. The results for SVD presented in Fig. 15d are erratic for orders of fit $n < 4$.

The basic anisotropy information is presented next in a series of composite plots, shown in Fig. 16a–d. The symmetry results are qualitatively similar to those obtained with the femur_1 image. In particular, the detected degree of anisotropy follows a similar trend: APS < MIL < SLD < SVD. Again, the detected principal triads, also shown, appear to be in reasonable agreement between descriptors.

Finally, the detected orientation triad is quantitatively assessed under different orders of fit. Fig. 17a–c show the principal fabric orientations plotted in angular coordinates for $n \in \{1, 2, \ldots, 5\}$. The primary and

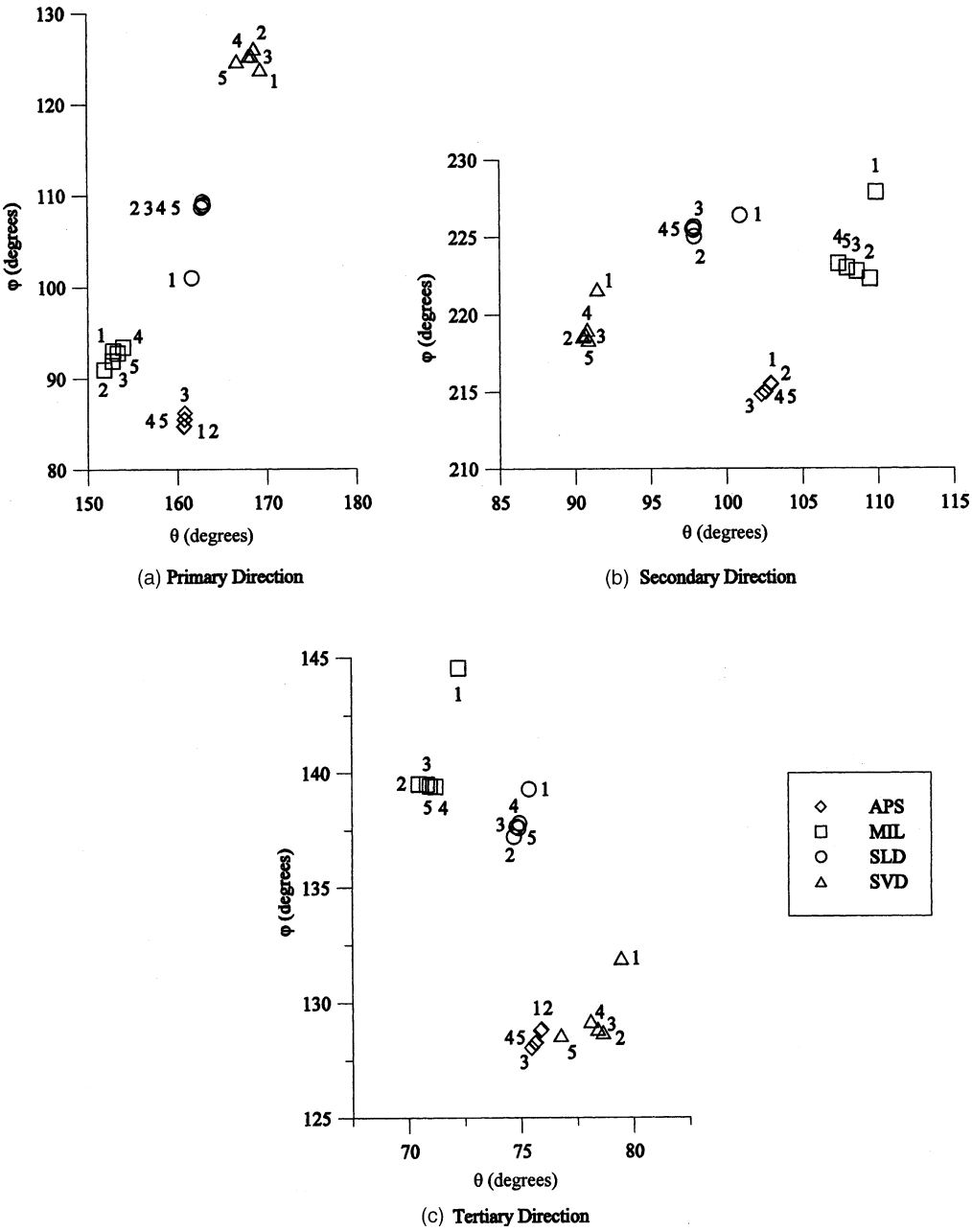

Fig. 14. Sensitivity of the orientation of principal directions of fabric to the order of fit; femur_1 image.

tertiary directions have been swapped in the case of APS for comparative evaluation with the other descriptors. In the case of APS and MIL descriptors, a stable configuration is obtained after a first-order fit while for SVD, consistent results are obtained with $n > 2$. SLD provides a reasonably stable configuration in the detected triad over the entire range of n.

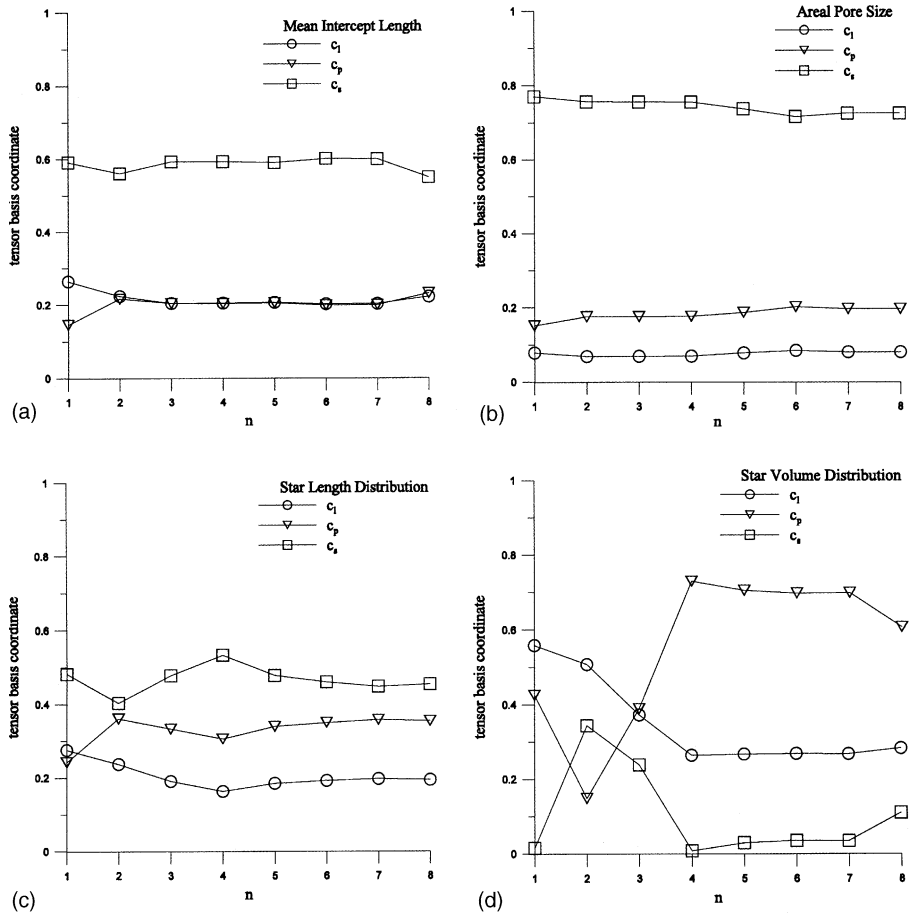

Fig. 15. Order of fit, n, versus tensor basis coordinates for various fabric descriptors; femur_2 image.

5. Final remarks

High resolution imaging techniques, such as μCT, provide the data from which 3D measurements of the porous microstructure of bone may be obtained. Specifically, from an arbitrarily oriented array of lineal probes passing through a binary data volume, the basic directionally dependent quantities can be identified which include: (i) the length of test lines intersecting the sampling volume; (ii) the sum of intercept lengths arising from the intersection of the test lines and the phase of interest; and (iii) the number of intercept lengths. In Section 2, the definitions of the descriptors MIL, SLD and SVD, were given in terms of these quantities and a new measure of fabric, known as *areal pore size*, was introduced.

Algorithms were developed for locating the intersections of both uniformly and non-uniformly spaced arrays of test lines with a prescribed phase of interest within a sampling domain of simple geometric shape. Specifically, algorithms for obtaining APS, MIL, SLD and SVD measurements using the line array approach were defined. Exhaustive and time-consuming approaches to sampling (i.e., random orientations) were avoided in favour of a uniform spatial sampling method known as the *generalized spiral points method*. Given a sufficient number of discrete measurements, an appropriate distribution function can be fit to

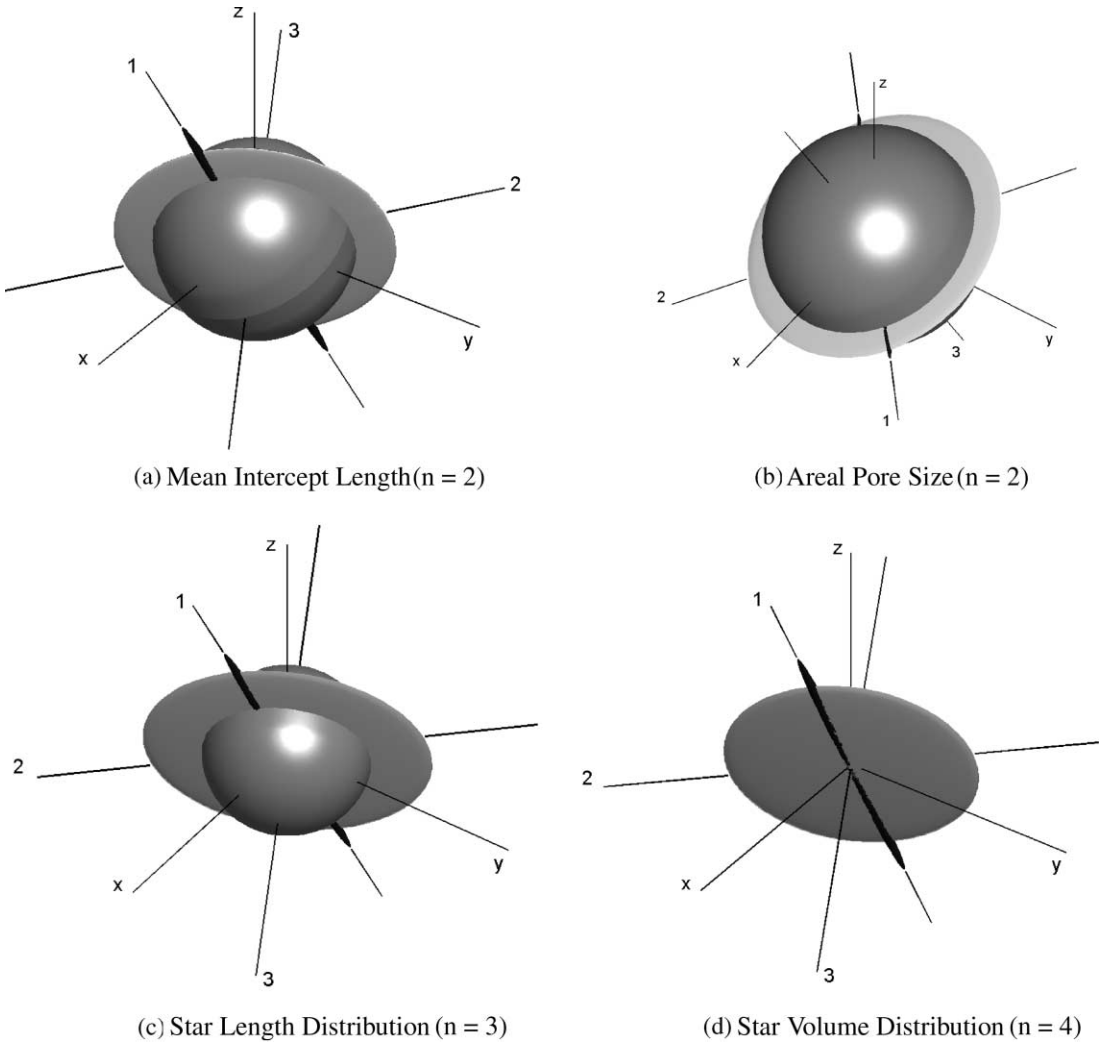

Fig. 16. Geometric representation of different fabric descriptors; femur_2 image: (a) mean intercept length ($n = 2$); (b) area pore size ($n = 2$); (c) star length distribution ($n = 3$); (d) star volume distribution ($n = 4$).

the data. By incorporating dyadic products of a second-order tensor, rather than pursuing higher-order tensor representations, a sufficient degree of accuracy can be achieved while maintaining orthotropic symmetry.

Different fabric descriptors have been examined over the course of the analysis discussed in Section 4. Based on this analysis, it is recommended that a range of order of fit be tried and assessed by a normalized goodness of fit measure, such as the χ^2 merit function. In general, the range of order of fit for which no significant further reduction in χ^2 is observed (i.e., generally for $n > 1$) tends to provide stable eigenvalues and principal orientations. In the case of the trabecular bone images considered here, a second-order fit is sufficient to produce reliable fabric information for most descriptors. In cases where significant fluctuations in the data are observed, an increase in the sampling resolution should be applied and the resulting measurements re-assessed in terms of tensor basis coordinate and principal triad angle plots. Once a suitable fit

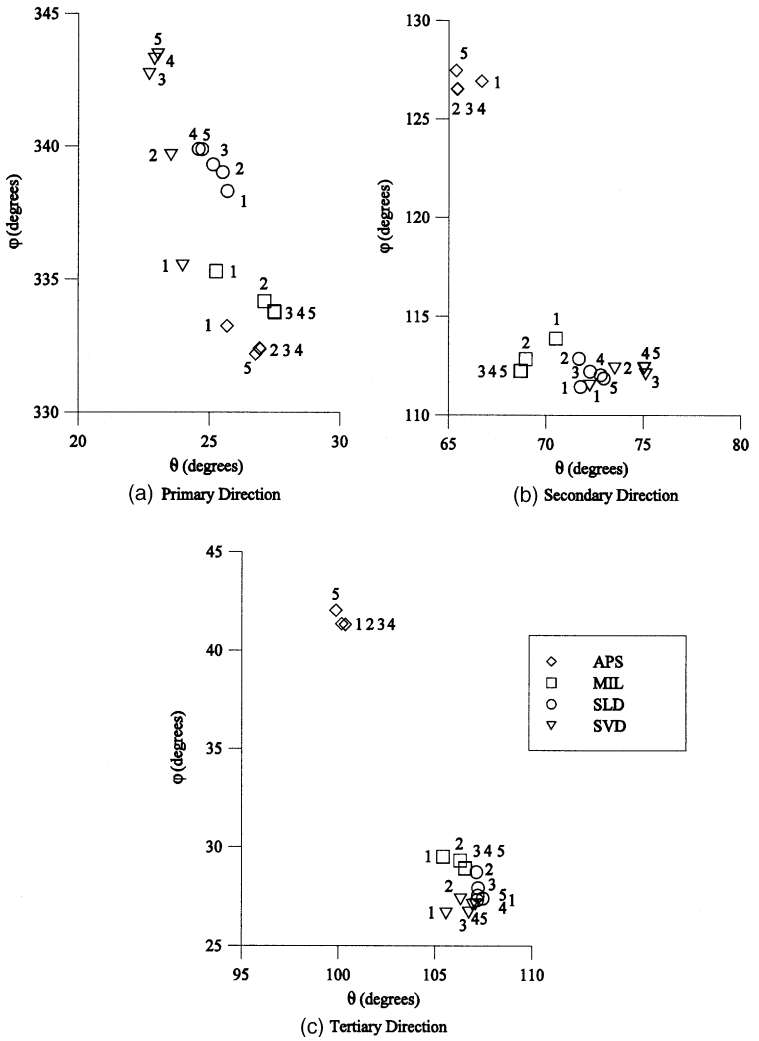

Fig. 17. Sensitivity of the orientation of principal directions of fabric to the order of fit; femur_2 image.

to the data is chosen, composite shape plotting provides an unambiguous graphical representation of both the material symmetry and the detected principal triad.

The results of the analyses suggest that some descriptors perform better than others in terms of detecting material fabric. SVD appears to overestimate the anisotropy information and, as shown in the principal plane plots in Fig. 10, the distribution of data is erratic when compared to other descriptors (e.g., SLD Fig. 11). At the same time, however, the detection of principal orientations by SVD is comparable in accuracy to that obtained with the other fabric measures. The degree of anisotropy, assessed in terms of the different descriptors, follows the general trend: MIL < APS < SLD < SVD. Similar observations have been reported by Smit et al. (1998). In terms of performance characteristics, APS consistently generated a smooth measurement response which may be attributed to the additional sample averaging around the main pole direction.

References

Chung, H.W., Wehrli, F.W., Williams, J.L., Kugelmass, D., Wehrli, S., 1995. Quantitative analysis of trabecular micro structure by 400 MHz magnetic resonance imaging. Journal of Bone and Mineral Research 10, 803–811.

Cohen, D., 1994. Voxel traversal along a 3D line. In: Heckbert, P.S. (Ed.), Graphics Gems IV. AP Professional, Cambridge, MA, pp. 366–369.

Cruz-Orive, L.M., Karlsson, L.M., Larsen, S.E., Wainschtein, F., 1992. Characterizing anisotropy: a new concept. Micron Microscopica Acta 23, 75–76.

Harrigan, T.P., Mann, R.W., 1984. Characterization of micro structural anisotropy in orthotropic materials using a second rank tensor. Journal of Material Science 19, 761–767.

Kanatani, K., 1984. Distribution of directional data and fabric tensors. International Journal of Engineering Science 22 (2), 149–164.

Kanatani, K., 1985a. Procedures for stereological estimation of structural anisotropy. International Journal of Engineering Science 23 (5), 587–598.

Kanatani, K., 1985b. Measurement of crack distribution in a rock mass from observation of its surfaces. Soils and Foundations 25 (1), 77–83.

Kuo, A.D., Carter, D.R., 1991. Computational methods for analyzing the structure of cancellous bone in planar sections. Journal of Orthopaedic Research 9, 918–931.

Myers, R.M., 1990. Classical and Modern Regression with Applications, second ed. PWS-KENT Publishing Company, Boston.

Oda, M., 1972. Initial fabrics and their relation to mechanical properties of granular materials. Soils and Foundations 12, 7–18.

Odgaard, A., Jensen, E.B., Gundersen, H.J.G., 1990. Estimation of structural anisotropy based on volume orientation. A new concept. Journal of Microscopy 157, 149–162.

Odgaard, A., 1997a. Three-dimensional methods for quantification of cancellous bone architecture. Bone 20, 315–328.

Odgaard, A., Kabel, J., Rietbergen, B., Dalstra, M., Huiskes, R., 1997b. Fabric and elastic principal directions of cancellous bone are closely related. Journal of Biomechanics 30, 487–495.

Pietruszczak, S., Inglis, D., Pande, G.N., 1999. A fabric-dependent fracture criterion for bone. Journal of Biomechanics 32, 1071–1079.

Pietruszczak, S., Mroz, Z., 2001. On failure criteria for anisotropic cohesive-frictional materials. International Journal for Numerical and Analytical Methods in Geomechanics 25, 509–524.

Rakhmanov, E.A., Saff, E.B., Zhou, Y.M., 1994. Minimal discrete energy on the sphere. Mathematical Research Letters 1, 647–662.

Saff, E.B., Kuijlaars, A.B.J., 1997. Distributing many points on a sphere. The Mathematical Intelligencer 19 (1), 5–11.

Sasov, A.Y., 1987. Microtomography—methods and equipment. Journal of Microscopy 147, 169–178, 179–192 (Parts I and II).

Sasov, A.Y., Van Dyck, D., 1998. Desktop X-ray microscopy and microtomography. Journal of Microscopy 191, 151–158.

Smit, T.H., Schneider, E., Odgaard, A., 1998. Star length distribution: a volume-based concept for the characterization of structural anisotropy. Journal of Microscopy 191 (pt. 3), 249–257.

Underwood, E.E., 1970. Quantitative Stereology. Addison-Wesley, New York.

Westin, C.F., Maier, S.E., Khidhir, B., Everett, P., Jolesz, F.A., Kikinis, R., 1999. Image processing for diffusion tensor magnetic resonance imaging. In: Taylor, C., Colchester, A. (Eds.), Medical Image Computing and Computer Assisted Intervention MICCAI'99, Proceedings. Springer, Berlin, pp. 441–452.

Whitehouse, W.J., 1974. The quantitative morphology of anisotropic trabecular bone. Journal of Microscopy 101 (pt. 2), 153–168.

Zysset, P.K., Curnier, A., 1995. An alternative model for anisotropic elasticity based on fabric tensors. Mechanics of Materials 21, 243–250.